Reconfigurable Hyperbolic Polaritonics with Correlated Oxide Metasurfaces

Neda Alsadat Aghamiri
University of Georgia

Guangwei Hu
National University of Singapore https://orcid.org/0000-0002-3023-9632

Alireza Fali
University of Georgia

Zhen Zhang
Purdue University

Jiahan Li
Kansas State University https://orcid.org/0000-0002-5118-0908

Sivacarendran Balendhran
University of Melbourne https://orcid.org/0000-0002-4390-3491

Sumeet Walia
RMIT University https://orcid.org/0000-0002-3645-9847

Sharath Sriram
RMIT University

James Edgar
Kansas State University https://orcid.org/0000-0003-0918-5964

Shriram Ramanathan
Purdue University

Andrea Alu
CUNY Advanced Science Research Center https://orcid.org/0000-0002-4297-5274

Yohannes Abate (YOHANNES.ABATE@uga.edu)
University of Georgia, Athens, Georgia 30602, USA

Article

Keywords: polaritons, optoelectronic devices, van der Waals crystals, nanophotonic applications

Posted Date: October 19th, 2021

DOI: https://doi.org/10.21203/rs.3.rs-947391/v1

Version of Record: A version of this preprint was published at Nature Communications on August 3rd, 2022. See the published version at https://doi.org/10.1038/s41467-022-32287-z.

Reconfigurable Hyperbolic Polaritonics with Correlated Oxide Metasurfaces

Neda Alsadat Aghamiri[1], Guangwei Hu[2,3], Alireza Fali[1], Zhen Zhang[4], Jiahan Li[5], Sivacarendran Balendhran[6], Sumeet Walia[7,8], Sharath Sriram[8,9], James H. Edgar[5], Shriram Ramanathan[4], Andrea Alù[2,10], Yohannes Abate[1*]

1 Department of Physics and Astronomy, University of Georgia, Athens, Georgia 30602, USA

2 Photonics Initiative, Advanced Science Research Center, City University of New York, New York, NY 10031, USA

3 Department of Electrical and Computer Engineering, National University of Singapore, Kent Ridge, Singapore 117583, Singapore

4 School of Materials Engineering, Purdue University, West Lafayette, IN 47907, USA

5 Tim Taylor Department of Chemical Engineering, Kansas State University, Manhattan, KN 66506, USA

6 School of Physics, University of Melbourne, Parkville, Victoria 3010, Australia

7 School of Engineering RMIT University Melbourne, Victoria, Australia

8 Functional Materials and Microsystems Research Group and the Micro Nano Research Facility RMIT University Melbourne, Victoria, Australia

9 ARC Centre of Excellence for Transformative Meta-Optical Systems, RMIT University, Melbourne, Victoria, Australia

10 Physics Program, Graduate Center, City University of New York, New York, NY 10016, USA

e-mail: yohannes.abate@uga.edu

Abstract

Polaritons enable subwavelength confinement and highly anisotropic flows of light over a wide spectral range, holding the promise for applications in modern nanophotonic and optoelectronic devices. However, to fully realize their practical application potential, facile methods enabling nanoscale active control of polaritons are needed. Here, we introduce a hybrid polaritonic-oxide heterostructure platform consisting of van der Waals crystals, such as hexagonal boron nitride (hBN) or alpha-phase molybdenum trioxide (α-MoO_3), transferred on nanoscale oxygen vacancy patterns on the surface of prototypical correlated perovskite oxide $SmNiO_3$ (SNO). Using a combination of scanning probe microscopy and infrared nanoimaging techniques, we demonstrate nanoscale real-time reconfigurability of complex hyperbolic phonon polaritons patterned at the nanoscale with unmatched resolution. Hydrogenation and temperature modulation allow spatially localized conductivity modulation of SNO nanoscale patterns, enabling robust real-time modulation and nanoscale reconfiguration of hyperbolic polaritons. Our work paves the way towards nanoscale programmable metasurface engineering as a new paradigm for reconfigurable nanophotonic applications facilitated by a hybrid material platform exploiting extreme light-matter interactions in polaritonic systems.

Introduction

Polaritons are hybrid light-matter particles that offer tremendous promise to manipulate light at subwavelength scales [1-3]. Advances in hybridizing polaritonic materials with optically active systems and correlated oxides have recently attracted widespread attention due to their ability to achieve novel functionalities that are actively tunable. For example, tunable polaritonic metasurfaces have been pursed for reconfigurable nano-optic functionalities in compact devices [4,5]. One strategy is to utilize phase-change media as a substrate to reconfigure van der Waals nanomaterials, thus modulating the supported phonon polaritons (PhPs) [4]. For instance, hyperbolic PhPs (HPhPs), featuring an extremely anisotropic dispersion that results in hyperbolic iso-frequency contours associated with associated large light-matter interactions can be manipulated with phase change substrates [4,6,7]. So far, such tunable polaritons have

relied on temperature[8-11] modulation, which introduces loss, as the phonon lifetime is reduced when the temperature, and correspondingly the phonon-phonon scattering events, increase. In addition, this route suffers from inaccessibility of nanoscale manipulation due to the inability to design localized thermal manipulation. As a result, reconfigurability of nanopolaritonic structures remains limited.

Correlated oxides provide exciting opportunities to reconfigure polaritonic devices at the nanoscale, due to their highly tunable optical and electronic properties [12-14]. Among these, rare-earth nickelates (RNiO$_3$, R = rare-earth element) display a rich phase diagram of structural and physical properties [15-18], controllable through various approaches, including doping [19,20] , temperature [21] , atomic vacancies [22] , electric bias [23] , and more. Hence, they have been investigated for reconfigurable nanoelectronics, fuel cells, and memristor devices [20,23-26]. As an example, the functional properties of SmNiO$_3$ (SNO) are extremely sensitive to the orbital occupancy of electrons via carrier doping [23,27,28], exhibiting a giant change – more than eight orders of magnitude – in resistivity, as well as an order of magnitude in optical bandgap at its hydrogen-doping driven Mott transition [28]. These properties enable SNO to reversibly change its refractive index over a broad frequency range, which has been explored for nanophotonic applications including electro-optic modulators for controllable scattering [28], while other opportunities remain unveiled.

Here, we demonstrate correlated oxide polaritonic meta-structures with on-demand and multimode programming of the supported polaritons at the nanoscale, achieved through field generated oxygen vacancies, hydrogen doping, as well as temperature modulation. We first present the characterization and manipulation of optical properties of SNO, then we demonstrate case studies of two prototypical hyperbolic van der Waals crystals, hexagonal boron nitride (hBN) [29-31]and alpha-phase molybdenum trioxide (α-MoO$_3$)[32,33 34], showcasing rich dispersion tuning of HPhPs and enabling diverse control and patterning of PhPs. Our results reveal unique opportunities for real-time nanoscale tunability of nanophotonic devices, thus advancing reconfigurable and programmable nanophotonic technologies.

Results and Discussions

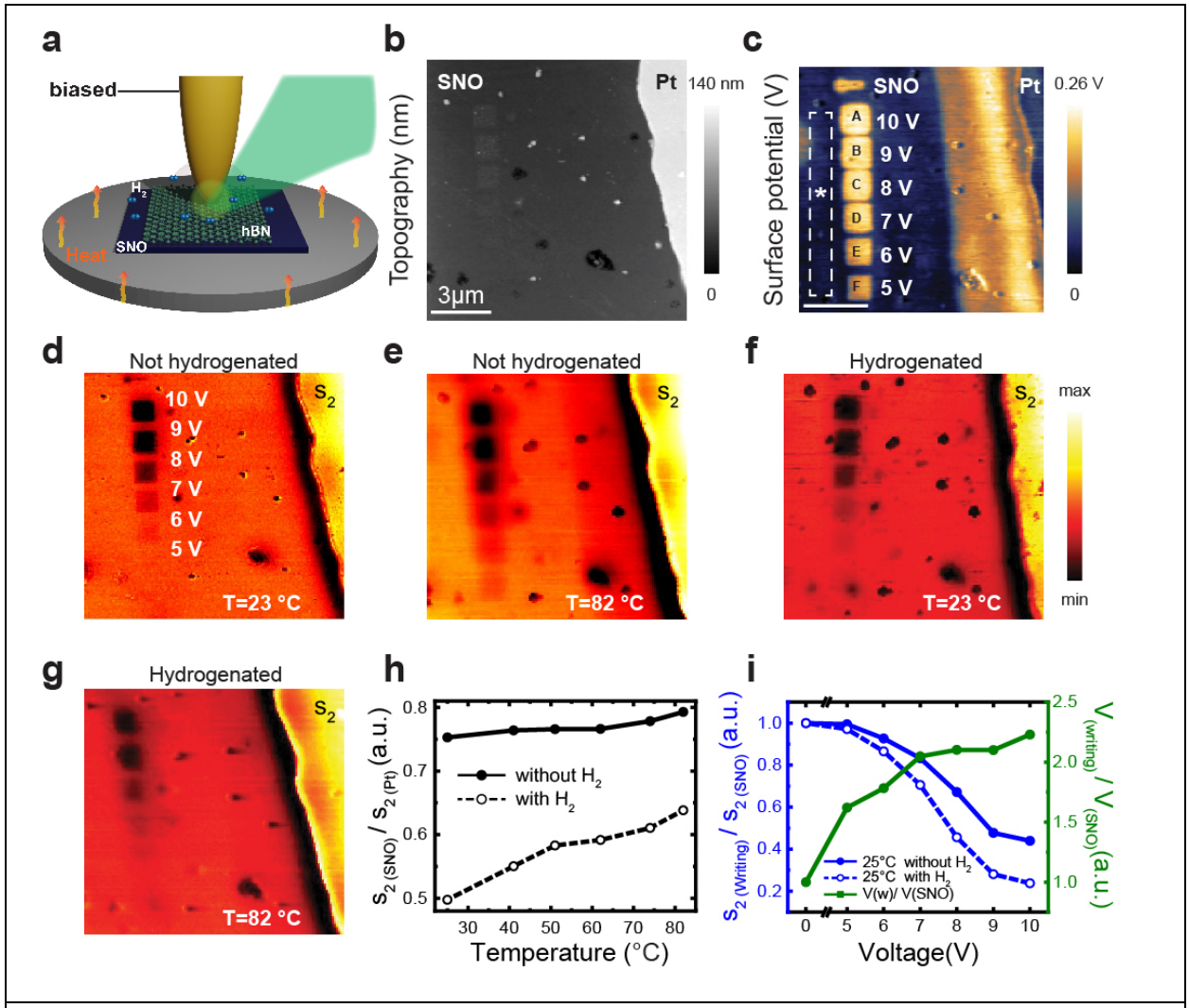

Fig. 1 | Tailoring the local conductivity of SNO. a, Schematics of integrated s-SNOM and heating setup. **b**, in case of conductive writing tip is biased. AFM topography image of pristine SNO. **c**, KPFM surface potential image of conductive writing patterns on pristine SNO made by applying 5V-10V potential at the c-AFM tip, corresponding IR s-SNOM second harmonic near-field amplitude s_2 images at **d**, T=23 °C (no H_2 exposure) **e**, T=82 °C (no H_2 exposure) **f**, T=23 °C, after exposing to 5% H_2 gas at 100 °C **g**, T=82 °C, after exposing to 5% H_2 gas at 100 °C. All samples were imaged at λ= 10.5 μm. **h**, Normalized amplitude plots with and without H_2 exposure. **i**, Normalized amplitude plots with and without H_2 exposure at T=25 °C (blue lines) and normalized potential plot of regions A-F (green line) as a function of voltage. All data points of plots were taken at regions with different potential (A-F) shown in panel c, and reference to normalize amplitude data is taken at * in panel c.

Scale bars indicate 3 μm.

We consider nanostructured surfaces based on SNO grown by magnetron co-sputtering on a $LaAlO_3$ substrate, and subsequently annealed in high pressure oxygen gas (see Methods for the detailed process). We first experimentally demonstrate multimodal hyperbolic metasurfaces by active lateral manipulation of electronic phases of SNO. To this end, we combine c-AFM and KPFM (Oxford Instruments) to generate and characterize patterns of various levels of conductivities on SNO. To write square charge patterns on a SNO sample (topography shown in Fig. 1b), we applied strong local fields via c-AFM operated in contact mode, detection set point 0.2 V, scan rate 0.5 Hz, and spring constant of the tip 2N/m. Subsequently, we mapped the surface potential of the written areas using KPFM operated in tapping mode with an amplitude of 500 mV (see Methods). The positive bias voltage in all writings leads to a large a potential compared to pristine SNO, as can be appreciated in the bright images in Fig. 1c. A tip with a large positive bias remove oxygen from the SNO near-surface region, providing a controllable route to manipulate the surface conductivity of SNO via the generation of oxygen vacancies [35]. This charge writing behavior is reversible with a negative bias [35]. Fig. 1h shows the potential distribution of the square writings ($V_{(writing)}$) normalized to the potential of pristine SNO ($V_{(SNO)}$), showing how the surface potential difference of the patterned areas increases with the tip bias voltage, commensurate with the change in local conductivity.

In order to quantitatively assess the local conductivity modulation of the charge writing process, we performed s-SNOM imaging of the patterned area of the sample. S-SNOM enables imaging local conductivity changes with high-sensitivity and high-spatial resolution, limited only by the sharpness of the probe tip (see Methods) [36-39]. The resulting s-SNOM amplitude images shown in Fig. 1d-g were taken at 10 μm laser wavelength and show the voltage-dependent optical contrast. Such s-SNOM image contrast directly reflects local conductivity changes [38] of the sample where dark regions, i.e., the area written with positive biases, imply lower conductivity compared to the pristine (red) region (Fig. 1d-g) due to the removal of oxygen from the SNO surface. Increasing the bias voltage decrease the local near-

field amplitude (local conductivity), as shown in the plot in Fig. 1i of the normalized amplitude, defined as the amplitude of the square writings ($s_{2(writing)}$) divided by the amplitude of the pristine SNO ($s_{2(SNO)}$). The combination of charge writing with c-AFM and optical imaging of local electronic changes by s-SNOM opens an exciting prospect for local conductivity lithographic patterning that could be of great interest in nanophotonics.

In addition to voltage control, the local conductivity of SNO can be tuned via temperature modulation or spontaneous hydrogenation, which also induce metal-insulator transition (MIT) [35]. We first investigate the temperature dependence of the pristine and charge written areas by mapping the near-field IR local response of the film. To this end, the sample was heated *in situ* at different temperatures on a custom-built heating stage integrated with the s-SNOM setup. After thermal equilibrium is reached (which is achieved by keeping the system at the selected temperature for 15 min), near-field images of the sample were acquired. In Fig. 1d and 1e, we show two amplitude images taken at room (23 ^{0}C) and high temperature (82 ^{0}C), respectively (see Fig. S1 for a series of images at other temperatures). Unlike most metals, for correlated oxides like SNO, increasing temperature or disorder does not hasten electron scattering processes; instead, increasing the temperature increase conductivity [40]. This is shown in Fig. 1h, which shows a linear normalized near-field amplitude plot as a function of temperature, revealing increasing amplitude, commensurate with increasing conductivity, as the temperature increases. However, the charge written areas do not show a similar trend, instead the measured change in normalized amplitude with temperature is weak (see Fig. S2) owing to reduced oxygen content. These dissimilar changes in conductivity between the pristine and charge written areas remarkably result in making the invisible charge written at low voltage (eg. 5 V) visible in s-SNOM amplitude images, as shown in Fig. 1e. Oxygen vacancies affect the electron occupancy (donate electrons to Ni-site e_g orbitals) and electron-electron correlation energy and band gap in SNO, which modulates the MIT behavior. S-SNOM images provide a direct and facile way to monitor these modulations.

Hydrogen dopants provide another robust route to dramatically modify the electronic phases of SNO [24]. We manipulate the local conductivity of pristine and charge written patterns of SNO by spontaneous hydrogen incorporation and then record in-situ the nanoscale changes via infrared s-SNOM imaging. The sample, with charge written and pristine areas, is exposed to H_2 using forming gas which is 5% H_2 and 95% N_2 for 30 minutes, while simultaneously heating the sample at 100 °C in a closed chamber. After hydrogen doping, the sample was cooled to room temperature and subsequent s-SNOM mapping was conducted as a function of temperature. Normalized amplitude s-SNOM plots of the pristine area of SNO as a function of temperature with and without hydrogen exposure are shown in Fig. 1h.The hydrogenated sample had a lower resistance than the pristine areas at all temperatures due to the modification of the electron configuration of e_g orbital of Ni in SNO [27]. A change in temperature also affects the charge written areas, resulting in a large increase of conductivity at high temperatures (Fig. S2).

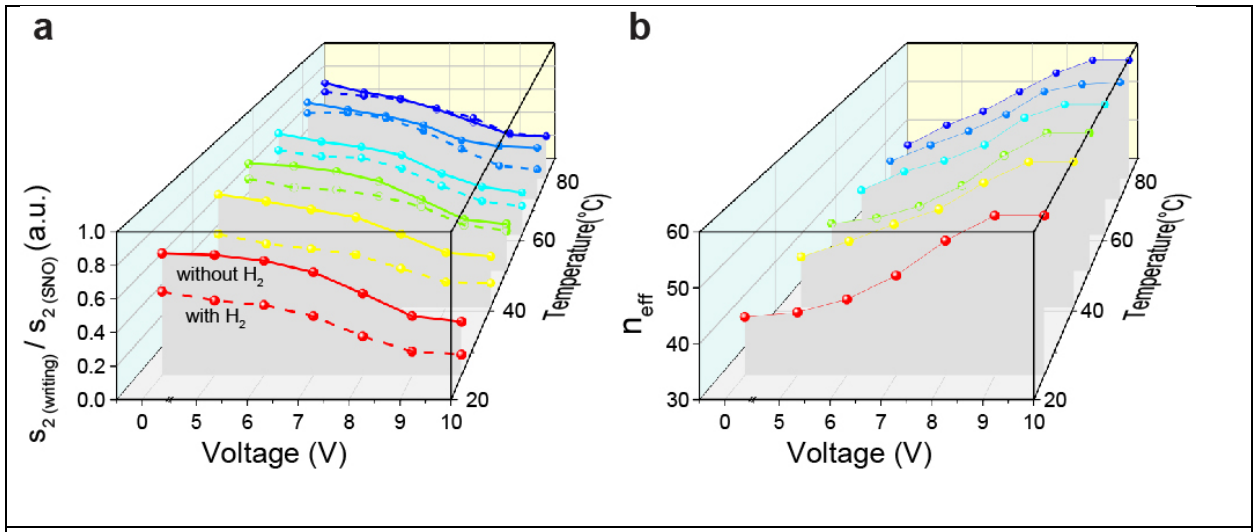

Fig. 2 | Local conductivity manipulation by controlling hydrogen dopants via applied field, temperature, and hydrogen incorporation. a, 3D plot showing changes in normalized amplitude $s_{2(writing)}/s_{2(SNO)}$ (z-axis) as a function voltage (x-axis) and temperature (y-axis) on a pristine and hydrogen doped SNO samples. Dashed lines represent data on a sample exposed to 5% H_2 and solid lines represent data on the pristine sample. **b**, Ratio of polariton wavevector to free space photon wavevector vs voltage and temperature.

Nanoscale reconfigurability of the local conductivity in correlated oxides enables manipulation of sub-diffraction light-matter interactions and unique opportunities to control propagating nano-confined polariton fields. Figure 2a summarizes the three independent knobs that enable nanoscale control of the local conductivity of SNO: oxygen vacancy control via tip voltage changes (x-axis), temperature (y-axis) and hydrogenation of the sample. Dashed lines represent normalized amplitude $s_{2(writing)}/s_{2(SNO)}$ on a sample exposed to 5% H_2 and solid lines represent data on pristine sample measured at various temperatures (shown by the different colors). As a case study to show the applicability of large tunability brought by the patterned SNO metasurfaces employing these knobs, we consider polaritons traveling in the [100] direction in an alpha-phase molybdenum trioxide (α-MoO_3) slab sandwiched between air and SNO, at the frequency ω=990.09 cm^{-1}. α-MoO_3 is an anisotropic van der Waals material, which has recently been explored for its unique polaritonic features [32,33,41-43]. In Fig. 2b we plot its effective index, n_{eff}, defined as k_ρ/k_0 along [100] direction, where k_ρ is the in-plane momentum of PhPs and $k_0 = 2\pi/\lambda$ is the momentum of light in free space with λ being the free-space wavelength of light. The plot shows how n_{eff} can be modified as temperature, voltage and hydrogen doping of SNO vary, which corroborates opportunities of tunable polaritonics based on correlated oxide metastructures, as further demonstrated below.

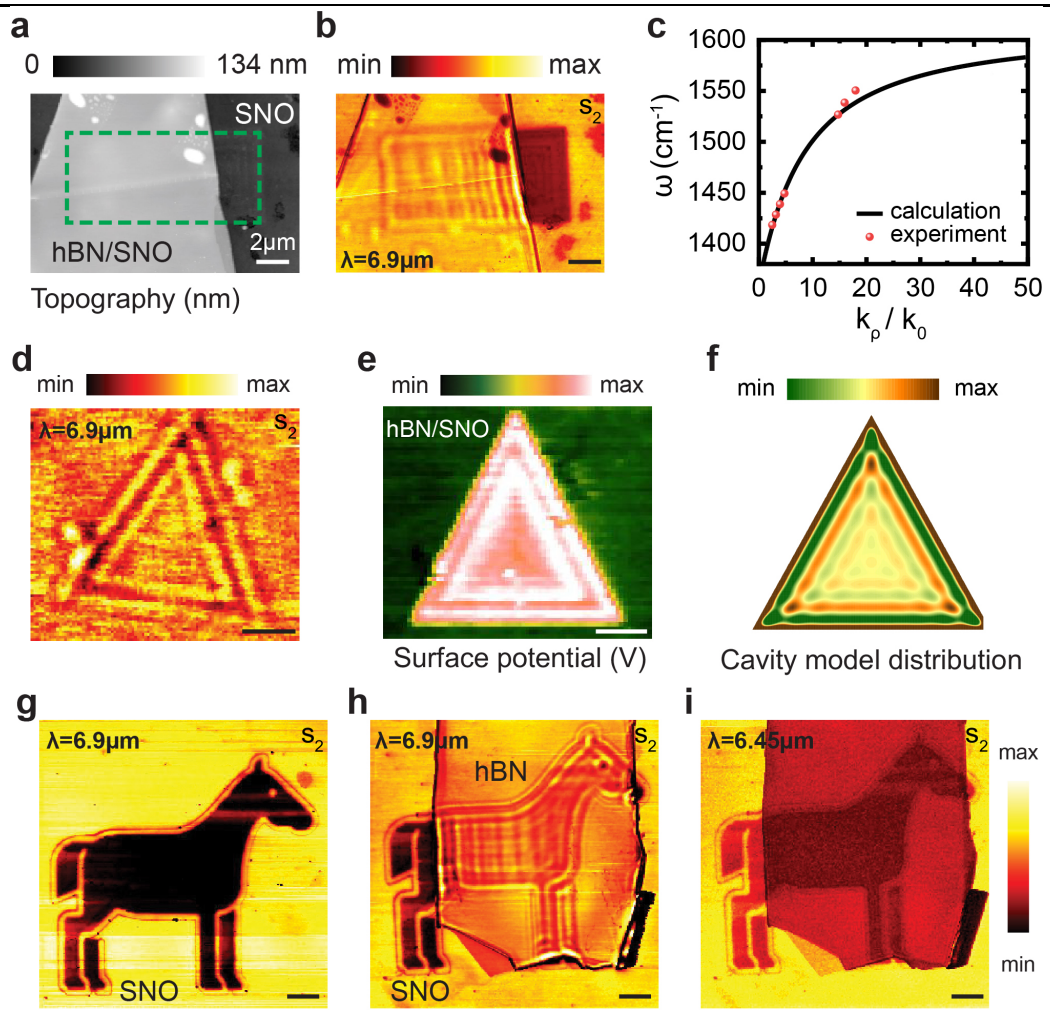

Fig. 3 | Tunable polaritonics with SNO-hBN architectures. a,Topographic image of pristine SNO, a lithography pattern is performed by applying 10 V potential at the c-AFM tip and a flake of 60 nm hBN (~99% boron-10 enriched) is transferred on top. **b**, IR s-SNOM second harmonic near field amplitude s_2 image. **c** Measurement of the dispersion relation of HPhPs in 60 nm thick hBN on SNO. **d**, Second-harmonic near-field amplitude s_2 image of a 60 nm hBN flake transferred on a triangular cavity lithographically patterned by applying a 10V potential c-AFM tip. **e** Corresponding KPFM surface potential images and **f**, simulation result (see Methods) for panel d. Second harmonic near field amplitude s_2 images of a lithographic pattern on SNO written by applying a 10V potential at c-AFM tip **g**, prior transferring a hBN flake and **h**, with a 50 nm thick hBN flake on top showing polaritons at 6.9 μm, and **i,** at 6.45 μm.

We now demonstrate nanoscale hyperbolic devices based on different SNO-hBN hybrid metasurfaces by introducing spatially localized dielectric variations of patterned geometries. We used boron-10 isotopically hBN (99 %) [4,30,44], a natural hyperbolic medium that supports low-loss bulk hyperbolic phonon polaritons (HPhPs) [30] exfoliated and then transferred on top of the SNO surface. Various size and shape patterns were written by applying a 5V-10V potential at the c-AFM tip. To demonstrate dispersion engineering, we first probe the polariton wavelength as a function of incident frequency with dielectric-like SNO, and then quantitatively extract modified HPhP dispersion. The lithography writing pattern (green dash lines in Fig. 3a) on the surface of SNO was obtained by applying 10V using c-AFM tip with a rectangular shape (6 μm x12μm); a 60 nm thick hBN (%99 enriched) was then transferred on its top covering both the writing and SNO pristine regions. We imaged HPhPs in the hBN using IR laser emitted by quantum cascade laser source focused on s-SNOM tip[45,46] (see Methods). Here, the AFM tip is used to launch polaritons and collect the polaritons reflected at local domain walls between insulating and metal phases of SNO. The evanescent fields induced at the tip apex launches HPhPs that propagate radially outward from the tip, confined within the volume of the hBN flake. Upon reaching the local pristine/charge written boundary, the HPhP is reflected and interferes with the outgoing mode to generate a pattern imaged by the s-SNOM tip as shown in Fig. 3b (a series of images are shown in Fig. S3). To capture the dispersion of the propagating HPhPs on the SNO surface, several incident laser frequencies are exploited. Accordingly, the dispersion relation can be retrieved, as shown by red dots in Fig. 3c, which agree well with our analytical model (solid black line in Fig. 3c, see Methods).

Next, we explore polaritonic cavity modes induced in reconfigurable SNO-hBN interfaces. Previous studies using patterned hBN such as nanoribbons [47,48] and nanocones [49] demonstrated resonant polaritons, but required demanding fabrication of insulating hBN. Here we offer an alternative facile patterning approach to realize reconfigurable polariton cavities, using spatially patterned SNO with a large contrast of conductivities. To this end, we realized a triangular cavity by applying 10V with c-AFM tip on SNO. Figures 3d and 3e show the near-field amplitude s_2 and surface potential SKPM images of the cavity, which agree with our numerical modeling (Fig. 3f). We model the modal polariton distribution in a

cavity, in this example a triangle shape, by the interference of polaritons reflected at the edges of the substrate cavity. The detailed modeling technique is provided in the Method section. Our results also show a sharp difference for polaritons propagating into and out of the triangle cavity (Fig. 3d), further confirming the distinct properties of SNO in different phases, and hence the large reconfigurability of polaritons. Moreover, different near-field images can be arbitrarily created via our modified SNO. Figures 3g and 3h show a pattern written on SNO imaged at 6.9 μm laser wavelength with and without hBN flake (thickness 50) on top of SNO, demonstrating the desired metasurfaces by imaging at the polariton wavelength (Fig. 3h) or outside the range of HPhP wavelength (Fig. 3i). These examples show that a simple tip-based high-resolution patterning of the oxide surface, instead of complicated fabrication of vdW materials themselves or substrates, can provide tailorable polariton cavities and other desired designs, allowing us to tailor on-demand reconfiguration of nanoscale hyperbolic polaritons.

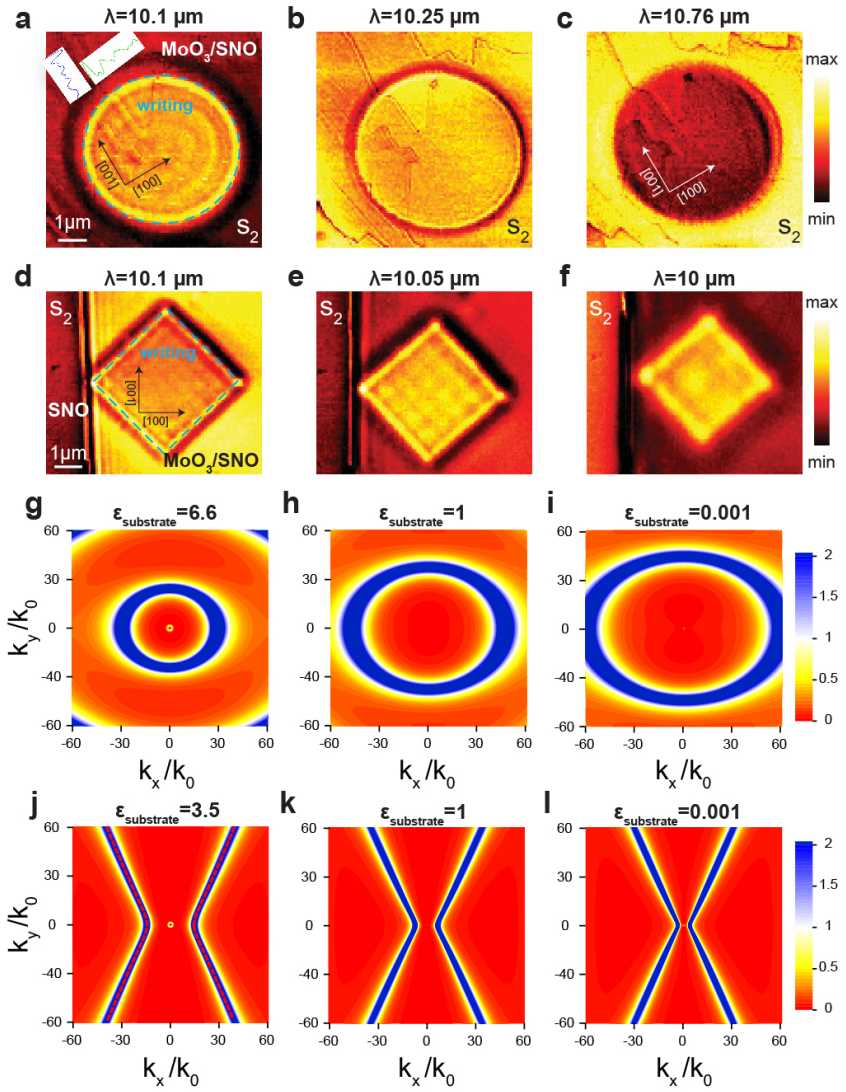

Fig. 4 | Tunable polaritonics with SNO-α-MoO_3 architectures. IR s-SNOM second-harmonic near field amplitude s_2 images of pristine α-MoO_3-SNO at **a**, λ=10.1 μm **b**, λ=10.25 μm and **c**, λ=10.76 μm. The lithography pattern (a circle with 5 μm diameter) was made by applying 10 V potential at the c-AFM tip and a flake of 120 nm α-MoO_3 is transferred on the top at part a, b and c. IR s-SNOM second harmonic near field amplitude s_2 images of pristine α-MoO_3-SNO at **d**, λ=10.1 μm **e**, λ=10.05 μm **f**, λ=10 μm, the lithography pattern (a square with 4 μm side) was made by applying 10 V potential at the c-AFM tip and a flake of 120 nm α-MoO_3 is transferred on the top at part a, b and c. **g-i**, Dispersion of polaritons for 100 nm thick α-MoO_3 on top of the correlated oxide metasurface with different permittivity, at the frequency of 990.09 cm^{-1}. **j-l**, Dispersion of hyperbolic polaritons for 100 nm thick α-MoO_3 on top of correlated oxide metasurfaces with different

permittivity, at the frequency of 900.9 cm^{-1}.

Tremendous recent interest has been focused on in-plane anisotropic PhPs in materials such as α-MoO_3 [32] [33], α-V_2O_5 [50] and others [51]. The dispersion of these materials can be engineered by intercalation [50,52,53], or rotation of multiple layers [42,54]. Here, we point to another avenue to realize tunable dispersion of in-plane anisotropic PhPs via largely tunable correlated oxide metasurfaces, a reconfigurable substrate that provides nanoscale on-demand dielectric patterns enabling the active manipulation of nano-confined fields. The structures were made by c-AFM with 10V bias, and α-MoO_3 was exfoliated and transferred on top of them (an anisotropic propagation of polaritons on hBN-SNO also were studied as shown in Fig. S4). Figure 4 shows hyperbolic polaritons in α-MoO_3 at different wavelengths. In Fig. 4a, we observe the elliptical shape with the largest PhP wavelength along the [001] (blue plot in Fig. 4a) and the smaller value along the [100] (green plot in Fig. 4a). More importantly, as we move to the L-RB (around 10.76 μm) the interference patterns show an almond shape (Fig. 4c) with the longest wavelength along the [100] and almost no propagation along the orthogonal [001] direction, which agrees with recent findings in this polaritonic platform [32]. Importantly, in these images, note that HPhPs mostly propagate inside the dielectric-phase SNO, with large confinement, while the fringe periodicities are dramatic different inside and outside the SNO circles. Furthermore, in Fig. 4 d-f the hyperbolic modes on square patterns that are twisted 45° angle from the sample axis [001], as shown in Fig. 4d for the 10.1, 10.05 and 10 μm laser wavelength respectively. HPH reflecting from edges propagate with almost the same wavelength at L-RB, while at the twisted angle of 45° with respect to the [001] axis the anisotropy is not found, consistent with recent findings using α-MoO_3 nanocavities [41] and suggesting highly reconfigurable nanocavities using shaped dielectric substrates. Our correlated oxide metasurfaces unlock broad opportunities for tunable polaritonic meta-devices. To further demonstrate the great promise of their application in tunable polaritonics, we plot the analytical isofrequency polariton dispersion for 100 nm thick α-MoO_3 on top of correlated oxide metasurfaces with different values of permittivity, as shown in Fig. 4g-l. The large changes of momentum in different Reststrahlen bands of α-MoO_3 can be observed, suggesting large confinement of polaritons and different levels of light-matter interactions. Furthermore, topological

transitions may also be available, if we further extend the permittivity range of tunability to negative values, as demonstrated in recent findings of α-MoO_3 on top of negative-permittivity substrates [55,56], which may be studied in future work.

Conclusion

In summary, nanoscale conductive regions were created on correlated prototypical perovskite SNO, and used demonstrate reconfigurable hyperbolic and anisotropic phonon polariton metasurfaces. A combination of c-AFM, KPFM and s-SNOM enabled us to generate and characterize nanoscale patterns with different conductivities values on SNO which were further tuned via temperature modulation and spontaneous hydrogenation. Nanoscale reconfigurable conductivity control in SNO enabled manipulation of sub-diffraction light matter interaction and dispersion engineering of desired HPhPs patterns in a direct and facile way. Our results demonstrate the tremendous potential of tunable correlated oxides metasurfaces for future configurable and tailorable quantum materials technologies.

References

1 Kildishev, A. V., Boltasseva, A. & Shalaev, V. M. Planar Photonics with Metasurfaces. *Science* **339**, 1232009, doi:10.1126/science.1232009 (2013).

2 Yu, N. & Capasso, F. Flat optics with designer metasurfaces. *Nature Materials* **13**, 139-150, doi:10.1038/nmat3839 (2014).

3 Basov, D. N., Asenjo-Garcia, A., Schuck, P. J., Zhu, X. & Rubio, A. Polariton panorama. *Nanophotonics* **10**, 549-577, doi:doi:10.1515/nanoph-2020-0449 (2021).

4 Folland, T. G. *et al.* Reconfigurable infrared hyperbolic metasurfaces using phase change materials. *Nature Communications* **9**, 4371, doi:10.1038/s41467-018-06858-y (2018).

5 Xiong, L. *et al.* Programmable Bloch polaritons in graphene. *Science Advances* **7**, eabe8087, doi:doi:10.1126/sciadv.abe8087 (2021).

6 Li, P. *et al.* Reversible optical switching of highly confined phonon–polaritons with an ultrathin phase-change material. *Nature Materials* **15**, 870-875, doi:10.1038/nmat4649 (2016).

7 Chaudhary, K. *et al.* Polariton nanophotonics using phase-change materials. *Nature Communications* **10**, 4487, doi:10.1038/s41467-019-12439-4 (2019).

8 Basov, D. N., Fogler, M. M. & García de Abajo, F. J. Polaritons in van der Waals materials. *Science* **354**, doi:10.1126/science.aag1992 (2016).

9 Low, T. *et al.* Polaritons in layered two-dimensional materials. *Nature Materials* **16**, 182-194, doi:10.1038/nmat4792 (2017).

10 Fali, A. *et al.* Refractive index-based control of hyperbolic phonon-polariton propagation. *Nano letters* **19**, 7725-7734 (2019).
11 Q. Zhang, G. H., W. Ma, P. Li, A. Krasnok, R. Hillebrand, A. Alù, C.-W. Qiu. Interface optics with van der Waals polaritons. *Nature* (2021).
12 Catalano, S. *et al.* Rare-earth nickelatesRNiO3: thin films and heterostructures. *Reports on Progress in Physics* **81**, 046501, doi:10.1088/1361-6633/aaa37a (2018).
13 Rensberg, J. *et al.* Active Optical Metasurfaces Based on Defect-Engineered Phase-Transition Materials. *Nano Letters* **16**, 1050-1055, doi:10.1021/acs.nanolett.5b04122 (2016).
14 Kats, M. A. *et al.* Ultra-thin perfect absorber employing a tunable phase change material. *Applied Physics Letters* **101**, 221101, doi:10.1063/1.4767646 (2012).
15 Hwang, J. *et al.* Structural origins of the properties of rare earth nickelate superlattices. *Physical Review B* **87**, 060101, doi:10.1103/PhysRevB.87.060101 (2013).
16 Middey, S. *et al.* Physics of Ultrathin Films and Heterostructures of Rare-Earth Nickelates. *Annual Review of Materials Research* **46**, 305-334, doi:10.1146/annurev-matsci-070115-032057 (2016).
17 Johnston, S., Mukherjee, A., Elfimov, I., Berciu, M. & Sawatzky, G. A. Charge Disproportionation without Charge Transfer in the Rare-Earth-Element Nickelates as a Possible Mechanism for the Metal-Insulator Transition. *Physical Review Letters* **112**, 106404, doi:10.1103/PhysRevLett.112.106404 (2014).
18 Lorenz, M. *et al.* The 2016 oxide electronic materials and oxide interfaces roadmap. *Journal of Physics D: Applied Physics* **49**, 433001, doi:10.1088/0022-3727/49/43/433001 (2016).
19 Zhang, H.-T. *et al.* Beyond electrostatic modification: design and discovery of functional oxide phases via ionic-electronic doping. *Advances in Physics: X* **4**, 1523686 (2019).
20 Sun, Y. *et al.* Strongly correlated perovskite lithium ion shuttles. *Proceedings of the National Academy of Sciences* **115**, 9672-9677, doi:10.1073/pnas.1805029115 (2018).
21 Ha, S. D., Otaki, M., Jaramillo, R., Podpirka, A. & Ramanathan, S. Stable metal–insulator transition in epitaxial SmNiO3 thin films. *Journal of Solid State Chemistry* **190**, 233-237 (2012).
22 Kotiuga, M. *et al.* Carrier localization in perovskite nickelates from oxygen vacancies. *Proceedings of the National Academy of Sciences* **116**, 21992-21997, doi:10.1073/pnas.1910490116 (2019).
23 Shi, J., Ha, S. D., Zhou, Y., Schoofs, F. & Ramanathan, S. A correlated nickelate synaptic transistor. *Nature Communications* **4**, 2676, doi:10.1038/ncomms3676 (2013).
24 Zhou, Y. *et al.* Strongly correlated perovskite fuel cells. *Nature* **534**, 231-234, doi:10.1038/nature17653 (2016).
25 Zhang, Z. *et al.* Perovskite nickelates as electric-field sensors in salt water. *Nature* **553**, 68-72, doi:10.1038/nature25008 (2018).
26 Zhang, H.-T. *et al.* Perovskite nickelates as bio-electronic interfaces. *Nature Communications* **10**, 1651, doi:10.1038/s41467-019-09660-6 (2019).
27 Shi, J., Zhou, Y. & Ramanathan, S. Colossal resistance switching and band gap modulation in a perovskite nickelate by electron doping. *Nature Communications* **5**, 4860, doi:10.1038/ncomms5860 (2014).
28 Li, Z. *et al.* Correlated Perovskites as a New Platform for Super-Broadband-Tunable Photonics. *Advanced Materials* **28**, 9117-9125, doi:https://doi.org/10.1002/adma.201601204 (2016).
29 Dai, S. *et al.* Tunable Phonon Polaritons in Atomically Thin van der Waals Crystals of Boron Nitride. *Science* **343**, 1125-1129, doi:doi:10.1126/science.1246833 (2014).
30 Giles, A. J. *et al.* Ultralow-loss polaritons in isotopically pure boron nitride. *Nature Materials* **17**, 134-139, doi:10.1038/nmat5047 (2018).

31 Caldwell, J. D. *et al.* Photonics with hexagonal boron nitride. *Nature Reviews Materials* **4**, 552-567, doi:10.1038/s41578-019-0124-1 (2019).
32 Ma, W. *et al.* In-plane anisotropic and ultra-low-loss polaritons in a natural van der Waals crystal. *Nature* **562**, 557-562, doi:10.1038/s41586-018-0618-9 (2018).
33 Zheng, Z. *et al.* Highly Confined and Tunable Hyperbolic Phonon Polaritons in Van Der Waals Semiconducting Transition Metal Oxides. *Advanced Materials* **30**, 1705318, doi:https://doi.org/10.1002/adma.201705318 (2018).
34 Zheng, Z. *et al.* A mid-infrared biaxial hyperbolic van der Waals crystal. *Science Advances* **5**, eaav8690, doi:doi:10.1126/sciadv.aav8690 (2019).
35 Yan, F. *et al.* Local charge writing in epitaxial SmNiO3 thin films. *Journal of Materials Chemistry C* **2**, 3805-3811, doi:10.1039/C4TC00030G (2014).
36 Stiegler, J. M. *et al.* Nanoscale Infrared Absorption Spectroscopy of Individual Nanoparticles Enabled by Scattering-Type Near-Field Microscopy. *ACS Nano* **5**, 6494-6499, doi:10.1021/nn2017638 (2011).
37 Huth, F. *et al.* Nano-FTIR Absorption Spectroscopy of Molecular Fingerprints at 20 nm Spatial Resolution. *Nano Letters* **12**, 3973-3978, doi:10.1021/nl301159v (2012).
38 Aghamiri, N. A. *et al.* Hyperspectral time-domain terahertz nano-imaging. *Opt. Express* **27**, 24231-24242, doi:10.1364/OE.27.024231 (2019).
39 Fali, A. *et al.* Nanoscale Spectroscopy of Dielectric Properties of Mica. *ACS Photonics* **8**, 175-181, doi:10.1021/acsphotonics.0c00951 (2021).
40 Jaramillo, R., Ha, S. D., Silevitch, D. M. & Ramanathan, S. Origins of bad-metal conductivity and the insulator–metal transition in the rare-earth nickelates. *Nature Physics* **10**, 304-307, doi:10.1038/nphys2907 (2014).
41 Dai, Z. *et al.* Edge-oriented and steerable hyperbolic polaritons in anisotropic van der Waals nanocavities. *Nature Communications* **11**, 6086, doi:10.1038/s41467-020-19913-4 (2020).
42 Hu, G. *et al.* Topological polaritons and photonic magic angles in twisted α-MoO3 bilayers. *Nature* **582**, 209-213, doi:10.1038/s41586-020-2359-9 (2020).
43 Chen, M. *et al.* Author Correction: Configurable phonon polaritons in twisted α-MoO3. *Nature Materials* **19**, 1372-1372, doi:10.1038/s41563-020-0781-x (2020).
44 Vuong, T. Q. P. *et al.* Isotope engineering of van der Waals interactions in hexagonal boron nitride. *Nature Materials* **17**, 152-158, doi:10.1038/nmat5048 (2018).
45 Fei, Z. *et al.* Gate-tuning of graphene plasmons revealed by infrared nano-imaging. *Nature* **487**, 82-85 (2012).
46 Chen, J. *et al.* Optical nano-imaging of gate-tunable graphene plasmons. *Nature* **487**, 77-81 (2012).
47 Dolado, I. *et al.* Nanoscale Guiding of Infrared Light with Hyperbolic Volume and Surface Polaritons in van der Waals Material Ribbons. *Advanced Materials* **32**, 1906530, doi:https://doi.org/10.1002/adma.201906530 (2020).
48 Li, P. *et al.* Collective near-field coupling and nonlocal phenomena in infrared-phononic metasurfaces for nano-light canalization. *Nature Communications* **11**, 3663, doi:10.1038/s41467-020-17425-9 (2020).
49 Caldwell, J. D. *et al.* Sub-diffractional volume-confined polaritons in the natural hyperbolic material hexagonal boron nitride. *Nature Communications* **5**, 5221, doi:10.1038/ncomms6221 (2014).
50 Taboada-Gutiérrez, J. *et al.* Broad spectral tuning of ultra-low-loss polaritons in a van der Waals crystal by intercalation. *Nat Mater* **19**, 964-968, doi:10.1038/s41563-020-0665-0 (2020).
51 Dai, Z. *et al.* Artificial Metaphotonics Born Naturally in Two Dimensions. *Chemical Reviews* **120**, 6197-6246, doi:10.1021/acs.chemrev.9b00592 (2020).

52 Wu, Y. *et al.* Chemical switching of low-loss phonon polaritons in α-MoO3 by hydrogen intercalation. *Nature Communications* **11**, 2646, doi:10.1038/s41467-020-16459-3 (2020).
53 Wu, Y. *et al.* Efficient and Tunable Reflection of Phonon Polaritons at Built-In Intercalation Interfaces. *Advanced Materials* **33**, 2008070, doi:https://doi.org/10.1002/adma.202008070 (2021).
54 Hu, G., Krasnok, A., Mazor, Y., Qiu, C.-W. & Alù, A. Moiré Hyperbolic Metasurfaces. *Nano Letters* **20**, 3217-3224, doi:10.1021/acs.nanolett.9b05319 (2020).
55 Zhang, Q. *et al.* Hybridized Hyperbolic Surface Phonon Polaritons at α-MoO3 and Polar Dielectric Interfaces. *Nano Letters* **21**, 3112-3119, doi:10.1021/acs.nanolett.1c00281 (2021).
56 Duan, J. *et al.* Enabling propagation of anisotropic polaritons along forbidden directions via a topological transition. *Science Advances* **7**, eabf2690, doi:10.1126/sciadv.abf2690 (2021).
57 Li, J. *et al.* Single crystal growth of monoisotopic hexagonal boron nitride from a Fe–Cr flux. *Journal of Materials Chemistry C* **8**, 9931-9935, doi:10.1039/D0TC02143A (2020).

Methods

Scanning probe microscopy (SPM) is a general term which includes techniques with AFM which is sharp metal probe is used in tapping mode and contacted mode. We used the Cypher AFM (oxford instrument) to acquire c-AFM and SKPM. To make the lithography pattern using c-AFM (Fig. 1,2,3) a contacted mode AFM was performed while applying 5V-10V through the metal Ti/Ir coated tip (Asyelectric.01-R2 from Oxford). In c-AFM the current is passed through the tip and into a transimpedance amplifier and it converts current to a voltage.

Scanning Kelvin probe microscopy (SKPM) is a technique that detects the potential difference between the probe tip and the sample. This technique is based on the AC bias applied to the tip to produce an electric force on the cantilever which is proportional to the potential difference between the tip and the sample. Using an AC bias, the probe is driven electrically and the potential difference between the tip and the sample causes the probe to oscillate. These oscillations are then cancelled by a potential feedback loop and the voltage required to match the probe to the sample is recorded as the surface potential in the software.

A combination of s-SNOM and nano-FTIR is used to acquire topography, near-field images and IR nano-spectra of SNO sample prepared by PVD on $LaAlO_3$ substrates. The experimental setup (Fig. 1b, neaspec co.) is based on a tapping mode AFM with a cantilevered metal-coated tip that oscillates at a resonance

frequency, Ω~280 kHz and tapping amplitude of ~50 nm. Focused infrared laser on the metalized tip interacts with the sample, and the scattered light from this interaction is demodulated at higher harmonics $n\Omega$ of the tapping frequency and detected via phase modulation interferometer. Either a coherent broadband infrared beam in the frequency range 700-2100 cm^{-1} (for nano-FTIR) or a monochromatic IR laser (for s-SNOM) is focused by a parabolic mirror to the tip. For nano-FTIR operation, the backscattered near-field light from the tip-sample junction is detected via mixing with an asymmetric Fourier transform Michelson interferometer. This detection method enables recording of both the amplitude **s(ω)** and phase **φ(ω)** spectra of the backscattered light. To extract background free local near-fields, the detector signal is demodulated at a higher harmonic nΩ of the tip mechanical resonance frequency Ω. Normalized amplitude (s_n(sample)/s_n(reference)) and phase (φ_n(sample)-φ_n(reference)) IR near-field spectra are acquired by first taking reference spectrum on a reference area (silicon is used in these experiments), followed by taking spectra at desired positions of the sample. (see Methods for details).

Materials synthesis:

SNO: $SmNiO_3$ thin films were prepared using magnetron co-sputtering from pure Sm and Ni target at room temperature. The substrates were cleaned using acetone and isopropanol and dried by blowing N_2 gas. During deposition, the chamber was maintained at 5 mtorr with flowing 40sccm Ar and 10 sccm O_2 gas mixture. The sputtering power was set as 170 W (RF) for Sm and 85 W (DC) for Ni to obtain stochiometric ratio. The as deposited films were subsequently annealed at 500 ^{o}C for 24 h in high pressure oxygen gas at 1400 psi to forming the perovskite phase.

HBN: The hexagonal boron nitride crystal flakes were grown at atmospheric pressure using an iron-chromium solvent, isotopically-enriched boron-10 (>99% ^{10}B) and nitrogen. The crystal growth process was previously described in detail [57].

MoO_3: Bulk α-MoO3 crystals were synthesized via physical vapor deposition. Commercial MoO3 powder (Sigma-Aldrich) was evaporated in a horizontal tube furnace at 785°C and bulk crystals were deposited at 560 °C. The deposition was carried out in a vacuum environment, with argon as the carrier gas for vapor transport (1 Torr). Subsequently, the bulk crystals were mechanically exfoliated using adhesive tape and flakes were transferred on to 300 nm SiO2 on Si substrates for characterization.

Numerical modeling: To model the polaritonic distribution at position $\vec{r}$, we take the linear combination of the polaritons launched by the tip and that reflected by the edge, which should follow [41]

$$E(\vec{r}) = E_0(\vec{r}) + \sum_m |R| e^{i\phi_R} e^{-2ik_t d_j} E_0(\vec{r})$$

Here, the first term is the onsite polariton signals launched by the tip, and $|R|e^{i\phi_R}$ denote the reflection characteristic at the edge by its amplitude ($|R|$) and phase parameters (ϕ_R). The addition propagation length accounting for the polariton propagating to and reflected by the edge is included in the term $e^{-2ik_t d_j}$ where d_j is the distance between the examination position and the edge and k_t being in-plane complex polariton momentum. Here, for simplicity, we assume that $|R| = 1$ and the reflection phase shift is $\phi_R = 1.5\pi$, which is reasonable and gives a better fitting in main text.

Acknowledgments

N.A., A.F. and Y.A. acknowledge support from the Air Force Office of Scientific Research (AFOSR), Grant No. FA9559-16-1-0172 and National Science Foundation (NSF), Grant No. 1904097. G.H., A.A. have been supported by the Vannevar Bush Faculty Fellowship and the Air Force Office of Scientific Research MURI program. S.S. acknowledges the Australian Research Council for project support (CE200100010). S. R. acknowledges NSF DMR 1904081 for support. J.H.E and J.L. appreciate support for hBN crystal growth from the Office of Naval Research (ONR), award no. N00014-20-1-2474.

Author contributions

Y.A. and A.A. conceived and guided the experiments. N.A.A. and A.F. carried out the experiments. N.A. conducted the conductive writing experiments, flake transfer, and experimental data analysis. G.H. did the calculations for polariton dispersion. S.R. and Z.Z. synthesized thin films of $SmNiO_3$. J.H.E. and J.L. provided the hBN. S.S. and S.W. developed techniques for the synthesis of the α-MoO_3. All authors contributed to writing manuscript.

Competing interests

The authors declare no competing interests.

Additional information

Supplementary information

Supplementary Files

This is a list of supplementary files associated with this preprint. Click to download.

- Oct11SNONatureCommAghamiriSI.docx